ANNALS OF GEOPHYSICS, 69, 5, V557, 2026; doi:10.4401/ag-9559
OPEN ACCESS

Interpretation of Gravity Data of the Bromo-Tengger Volcanic Complex Based on Geostatistical Analysis

Anik Hilyah[1], Sismanto Sismanto[*,1], Mochamad Nukman[1]

(1) Universitas Gadjah Mada, Department of Physics, Yogyakarta, Indonesia

Article history: received March 18, 2026; accepted September 12, 2026

Abstract

An accurate gravity map provides fundamental data for geoscience research and enables accurate subsurface interpretation. For many years, prior gravity surveys in the Bromo-Tengger volcanic complex have been unsuccessful in accurately defining rock units, structural continuity, and caldera boundaries. This study analyzed a residual gravity anomaly map produced through geostatistical analysis to overcome these limitations, which forms the basis for subsequent geological interpretation. Geostatistical analysis revealed that the Gaussian variogram model best fits the residual gravity map. This model fulfilled the minimum residual sum of squares and a mean squared deviation ratio of 0.998, which is close to the ideal value of 1. This model produced a more precise image of the subsurface geology than previous studies and accurately identified previously unmapped positive anomalies on volcanic cones and visibly defined the boundaries of the Tengger Caldera, the Cemorolawang Wall lineament, and the estimated depth of the caldera basement. This study identified elevated residual gravity values in the Tengger volcanic rocks and lower values in the young cone complex pyroclastic deposits, which constitute the primary caldera-filling material. The interpretation of this study's results will contribute to future geoscience studies related to the Bromo-Tengger volcanic complex.

Keywords: Caldera; Gravity; Geostatistics; Variogram; Kriging

1. Introduction

Volcanic activity occurring at convergent plate boundaries leads to volcano formation along these boundaries. Indonesia has 147 volcanoes, 76 of which are classified as active volcanoes and are spread across the islands of Java, the Nusa Tenggara archipelago, Sumatra, and Sulawesi (Hariyono and Liliasari, 2018). The study area is located in the Bromo-Tengger volcanic complex in East Java, Indonesia. This volcanic complex was formed by a chain of mountains stretching across the island of Java, resulting from the subduction of the Indo-Australian plate beneath the Eurasian plate (Fig. 1) (Hall, 2002; Toulier, 2020).

In late 2015, Mount Bromo erupted for almost three months. This activity caused crop failures for 473 farmers, changed flight schedules, and emitted ash, which affected visibility in the surrounding area, traffic accidents, and negatively affected human health (Rachmawati et al., 2018; Venzke, 2016; Wardoyo et al., 2020). Mount Bromo has been monitored using various methods, such as remote sensing, geophysical measurements, ground deformation,

gas emissions, and visual observations, due to the risk and repeated eruption activity (Sukir et al., 2017). Several geophysical studies have investigated the subsurface, such as those conducted by Maryanto et al. (2017), who performed gravity measurements over three periods – 1997, 2001, and 2014 – to identify temporal changes in Bouguer anomalies in the Bromo-Tengger complex. The authors concluded that the changes in anomaly values were caused by the eruptive activity of Mount Bromo. Hilyah et al. (2017) studied soil vulnerability in the Tengger Caldera area using the microtremor method. The results of that study recommended gathering points and evacuation routes for disaster mitigation in the event of a Mount Bromo eruption. Lestari et al. (2017) studied the types of deposits in the Tengger Caldera using the resistivity method. The Tengger Caldera area is mostly composed of pyroclastic deposits of tuff and lapilli types. However, the study was limited to a depth of 2.15 m from the surface of the Tengger Caldera and, therefore, could not identify deeper rock units. Rochman et al. (2024) conducted another geophysical study using the magnetic method to map the distribution of rocks based on their magnetic properties. Low anomalies were found around the crater of Mount Bromo, which are likely associated with volcanic activity beneath the surface. Although these studies have depicted the distribution of several physical parameters in lateral cross-sections, they have not yet provided a detailed understanding of the geological features that form the Bromo-Tengger complex.

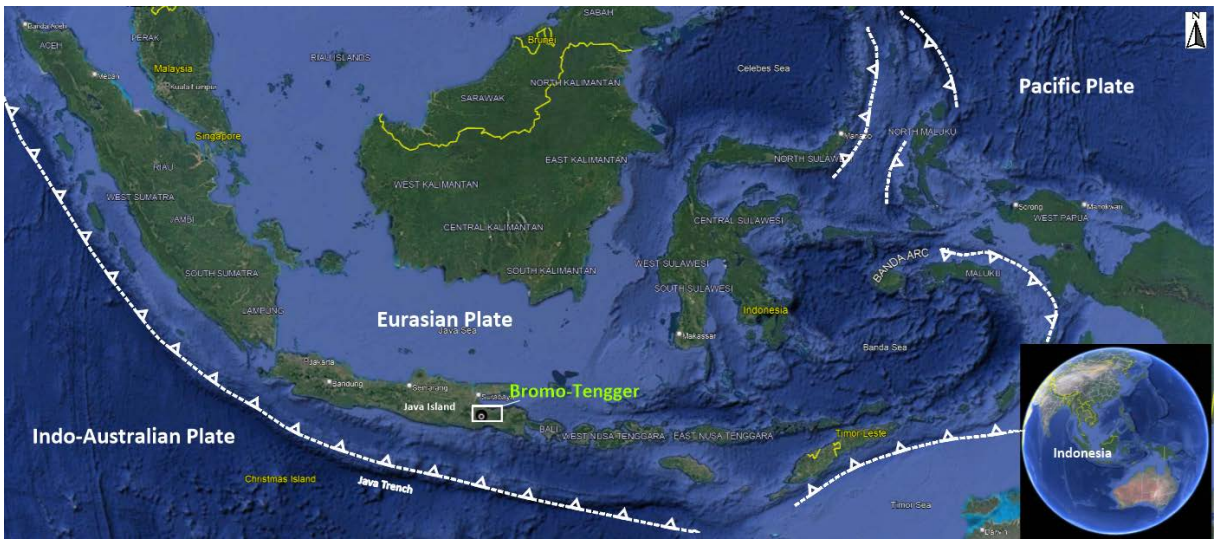

Figure 1. The study locations affected by the subduction of the Indo-Australian plate toward the Eurasian plate were modified from the study by Toulier et al. (2020). The subduction between the plates is indicated by the white lines.

The characteristics of the resulting anomalies and their relationship to subsurface geological conditions still require further research, and a comprehensive explanation of subsurface conditions has yet to be provided. Under these conditions, this study was conducted using a geological approach and gravity measurements to understand the correlation between geological conditions and gravity anomaly characteristics. This study uses satellite gravity data and geostatistical analysis to produce more accurate interpretations. Geostatistics is highly valuable for examining spatial variability, interpolating data between observation points, and generating interpolation maps by reducing errors through kriging interpolation (Gumiaux et al., 2003). Multiple studies have consistently demonstrated the effectiveness of geostatistics in analyzing geoscience data, indicating that geoscience data display spatial variation characteristics (Belkhiri et al., 2020). The application of geostatistics to the analysis of volcanic data has been well documented (Bellotti et al., 2010; Giustini et al., 2019; Heriawan et al., 2020; Sabrian et al., 2024), as has its application to gravity data (Njandjock et al., 2013; Valentin et al., 2012).

Various kriging methods, including simple kriging, ordinary kriging, indicator kriging, and co-kriging, have been extensively used to assess the spatial distribution of geoscience data variables (Xie et al., 2022). This study used ordinary kriging because of its suitability for single-variable analysis, unknown mean values, and the absence of data trends (Oliver and Webster, 2014). Ordinary kriging allows for more accurate interpolation by reducing estimation errors through proper variogram analysis. By using geostatistical analysis, this study produced a more

accurate residual gravity map that can serve as a reference for geoscience studies in the Bromo-Tengger volcanic complex, estimation of natural resource potential, and volcanic eruption hazard mitigation.

2. Study Area and Data Used

The Bromo-Tengger volcanic complex is a stratovolcano-type volcanic complex that is approximately 1.4million years old. The ancestral pre-caldera Tengger Volcano is estimated to have reached a height of approximately 4,500 m prior to its collapse (Van Gerven and Pichler, 1995), and the present-day caldera floor lies at an elevation of approximately 2,100 m. This complex comprises several volcanic cones located within the Tengger Caldera. The caldera spans an area of 7 × 8 km and was formed at the end of the Pleistocene and the beginning of the Holocene (Mulyadi, 1992). The eruption paths within the caldera form cones or rings of phreatomagmatic-andesitic tuff, consisting of Widodaren (Wjp), Kursi (Kujp), Segarawedi (Swjp), the Strombolian basalt cone Batok (Bajp), and Bromo (Bojp) (Fig. 2a). Volcanic activity in the study area includes igneous rocks and pyroclastic deposits (Hendrayana et al., 2024). The Ngadisari Caldera in the northeast, the Tengger volcanic rocks (Tdk) surrounding the caldera, and the remnants of the crater ridge of Mount Ijo in the western part of the caldera consist of layered igneous rocks, volcanic fallout material, and pyroclastic deposits. The Tengger Caldera comprises tephra and unconsolidated pyroclastic fall deposits formed as a result of volcanic activity following the formation of the Tengger Caldera (Abrory, 2019). The intra-caldera complex in Mount Bromo is influenced by the N-S fault line, which stretches from Semeru in the south to the Ranu Grati maar in the Pasuruan plain in the north (van Padang & Association, 1951). A NW-SE strike-slip fault influences the Cemorolawang Wall in the northeast of the Tengger Caldera. The faults within the Tengger Caldera are influenced by the faults surrounding the study area, as determined from the analysis of fault lines on a digital elevation model (DEM) map (Fig. 2b).

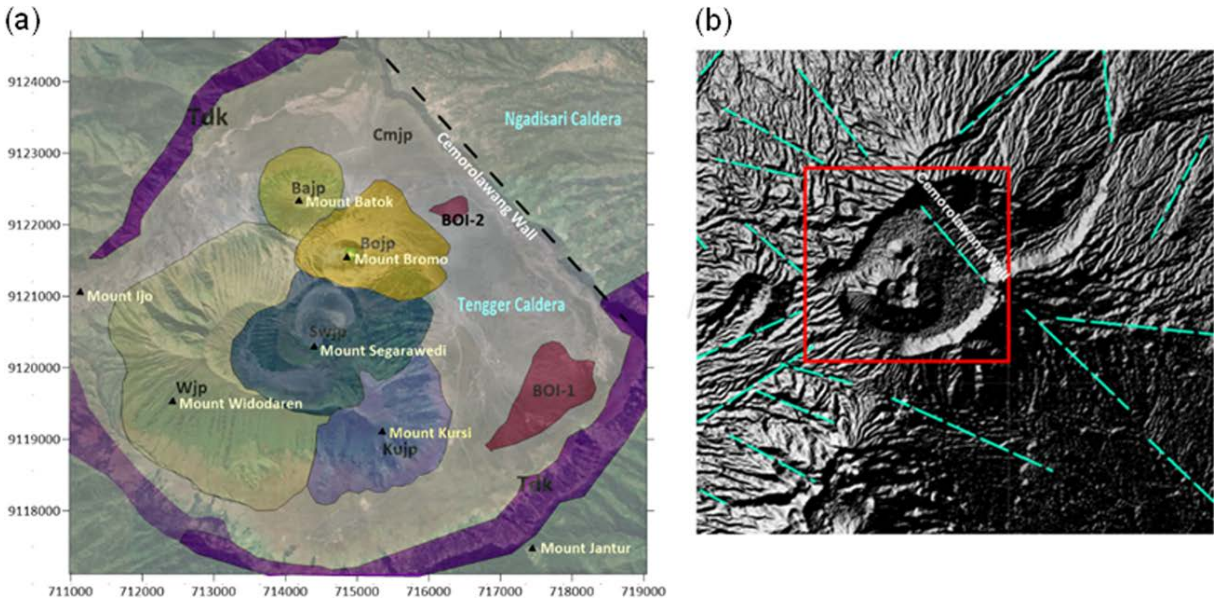

Figure 2. (a) Geological map of the Bromo-Tengger volcanic complex (Mulyadi, 1992); (b) Digital elevation model (DEM) map of the Bromo-Tengger area and its surroundings, where the study area is shown as a red box, and the green dashed line indicates the presence of a fault.

This study used data from the Global Gravity Model Plus (GGmPlus) 2013, which were downloaded from the website https://geodesy.curtin.edu.au/research/resolution/ on May 19, 2024. The data consisted of 306 gravity acceleration measurements with a resolution of 0.002° (7.2 arcseconds) and a distance of 400 m between the data points. Unlike models referenced to a constant flat datum, high-resolution global gravity models such as GGMplus 2013 compute surface gravity acceleration values directly on the actual undulating topographic surface (drape surface) to preserve short-wavelength features. In the Bromo-Tengger complex study area, these observation points were situated at

highly irregular elevations ranging from 1,869 m to 2,980 m. The IGSN71 gravity datum reference was used for the gravity measurements (Morelli et al., 1972). The free-air and Bouguer anomalies were computed using the GRS80 ellipsoid parameter reference (Moritz, 1980). A global free-air gradient of 0.3086 mGal/m was used for elevation correction. To ensure a rigorous removal of topographic effects across the steep and extreme relief of the volcanic complex, terrain correction was meticulously processed within the Geosoft Oasis montaj software environment. The correction utilized a high-resolution Shuttle Radar Topography Mission (SRTM) 1-arc second global digital elevation model (~30-meter spatial resolution) acquired from the USGS EarthExplorer. A robust hybrid calculation scheme was deployed to manage severe terrain changes. Nagy (1966) analytical formula for a right rectangular prism was applied to compute the immediate terrain cells in the inner zone, whereas Kane (1962) clustering algorithm was implemented to optimize and calculate the intermediate and outer regional zones up to a strict cutoff boundary of 20 km from each observation station. This cutoff radius reflects a deliberate compromise rather than a fully optimized solution; it focuses on excluding marine bathymetric areas and nearby large volcanic structures, which could create artificial density-contrast distortions and obscure local anomalies, rather than extending the correction to larger radii, where the CBA pattern would fully stabilize. A standard crustal reduction density of 2.67 g/cm^3 was used for both Bouguer and terrain corrections. This choice ensures seamless compatibility with the regional gravity mapping standards of Indonesia (Buyung et al., 1994) and maintains mathematical consistency during the joint analysis with satellite gravity datasets, thereby preventing artificial topography-correlated biases. Although this single-density approach has inherent limitations, any remaining correlation between the CBA and topography is attributed to genuine near-surface lithological variations rather than unresolved terrain effects. The basement rocks of the caldera consist of alternating andesitic-basaltic lava, volcanic breccia, and sandy tuff with a density of 2.4-2.8 g/cm^3 (Santamaria and Suwarti, 1992). The densities of the pyroclastic deposits and volcanic fallout material filling the caldera range from 1.9 to 2.2 g/cm^3 (Untung and Hasegawa, 1982). The density contrast between pyroclastic deposits and the underlying basement rocks often results in gravity anomalies that can be used to map features with densities higher or lower than those of the basement rocks.

3. Methodology

To provide a comprehensive overview of the reduction stages, anomaly separation, and subsurface modeling, the data processing workflow in this study systematically spans from initial satellite data preparation to integrated geological interpretation. Sequential geodetic and gravity corrections were applied to the raw data to eliminate non-geological effects and topographic influences. These processes included latitude correction to adjust for the Earth's rotation and ellipticity, free-air correction to compensate for the vertical elevation of the observation points above the reference ellipsoid, Bouguer correction using a standard crustal density assumption of 2.67 g/cm^3 to remove the mass effect between the datum and the observation level, and terrain correction based on Digital Elevation Model (DEM) data to mitigate the topographic effects surrounding the observation points. Given that satellite-derived data are inherently measured over an irregular surface, flat plane reduction was subsequently performed to project the data onto a uniform horizontal plane. This process was achieved using a dual-approach technique involving equivalent source plane modeling, followed by interpolation onto a uniform gridded horizontal plane.

The next stage involved the separation of deep regional and shallow residual anomalies using a moving average filter. To eliminate subjectivity in the filter configuration, the window size was quantitatively determined through 2D spectral analysis along several representative gravitational trajectories within the study area, following the method established by Spector and Grant (1970). This spectral analysis was performed by transforming the gravity anomaly data from the spatial domain to the frequency domain using the Fast Fourier Transform (FFT). Based on the natural logarithm plot of the amplitude against the wavenumber (k), two main slopes were identified, reflecting two distinct groups of anomalous source depths: the deep regional zone and the shallow residual zone. The critical cut-off wavelength (λ_c) parameter was determined through the inflection point between the linear regression segments of the regional and residual components. The spectral analysis yielded an average grid spacing of 76 m between grid nodes of the interpolated Gridded Horizontal Plane (GHP) and a cut-off wavelength (λ_c) of 503 m, mathematically resulting in a fractional value of $\approx 503/76 \approx 6.6$ grids. However, in 2D spatial signal processing computing, the filter operator matrix (filter kernel) must rest on odd integers to ensure that the matrix operator maintains a symmetrical center pixel component during the data convolution process. Rounding to the nearest odd integer, in this case,

rounded up to 7 was crucial for this symmetry. Therefore, the size of the window dimensions for the moving average filtering was definitively established at 7×7 grids, equivalent to a physical width of 7×76 m ≈ 532 m – closely matching the ≈503 m cut-off wavelength identified from the spectral analysis.

After separating the anomalies, the total horizontal derivative (THD) analysis was applied to the residual anomaly grid to objectively identify lineaments, density contrast boundaries, and the orientations of fault structures. THD is defined as $\mathrm{THD}(x, y) = \sqrt{(\partial g/\partial x)^2 + (\partial g/\partial y)^2}$, where g represents the residual gravity anomaly, and $\partial g/\partial x$ and $\partial g/\partial y$ are its first-order horizontal derivatives in the x and y directions, respectively, calculated numerically over the gridded anomaly surface (Grauch and Cordell, 1987). To produce a robust visualization of the spatial continuity of these anomalies, a comprehensive geostatistical analysis was conducted. This stage initiated with a quadratic transformation to normalize the data distribution, followed by the calculation of an experimental variogram and fitting it to the optimal variogram model. Anomaly values in unsampled areas were then interpolated using ordinary kriging. The predictive performance and mathematical accuracy of the interpolation model were rigorously evaluated using cross-validation metrics, specifically the residual sum of squares (RSS), residual mean square (RMS), and mean squared deviation ratio (MSDR). The final phase of this workflow involved integrated geological interpretation. This comprised delineating lithological units based on lateral density contrasts, identifying major structural elements using the boundaries enhanced by the THD analysis, and estimating basement depths via structural inversion modeling to map the geometry and morphology of the underlying subsurface basin.

4. Geostatistical Analysis

4.1 Variogram

In spatial interpolation, data points that are near each other typically exhibit more similarities than data points that are more distant. A variogram analysis was conducted to determine the extent to which the data influenced the estimation. This analysis assessed semivariance based on distance using a variogram. The variogram was derived from the following equation proposed by Matheron (1963):

$$\hat{\gamma}(h) = \frac{1}{2m(h)} \sum_{\alpha=1}^{m(h)} \{z(x_\alpha) - z(x_\alpha + h)\}^2 \tag{1}$$

The semivariogram is denoted by $\hat{\gamma}(h)$, $m(h)$ where m represents the count of data pairs spaced by a specific lag distance (h), and $z(x_\alpha)$ and $z(x_\alpha + h)$ indicate the data at points x_α and $(x_\alpha + h)$, respectively.

An experimental variogram was created from the data based on Eq. (1). Subsequently, the model variogram curve was adjusted to match the experimental variogram using the least-squares technique (Cressie, 1985; Zhang et al., 1995). The outcome of this curve-fitting process included geostatistical parameters, specifically, the nugget, range, and sill, which satisfy the following equation:

$$\begin{aligned} \gamma(h) &= c_0 + c\left\{\frac{3h}{2r} - \frac{1}{2}\left(\frac{h}{r}\right)^3\right\} && \text{for } 0 < h \leq r \\ &= c_0 + c && \text{for } h > r \\ &= 0 && \text{for } h = 0 \end{aligned} \tag{2}$$

A nugget (c_0) indicates uncorrelated variation at certain sampling distances, which can also be caused by measurement errors. Variance (c) represents the data spread, and range (r) shows the spatial correlation between the data at specific distances. Sill ($c_0 + c$) is the variance of the random process. The best-fitting variogram model demonstrates that spatial autocorrelation occurs among variables within a certain range. The experimental variogram was fitted using exponential, spherical, and Gaussian variogram models. These models are commonly applied in geosciences, and most geoscience data fit these models (Bohling, 2007). The variogram model that best fits the experimental variogram is selected for use in the next step of the geostatistical analysis.

4.2 Ordinary Kriging

Ordinary kriging is a geostatistical interpolation technique that provides the best linear unbiased estimate by relying on spatially dependent variance (Goovaerts, 1997). The ordinary kriging equation generally takes the following form:

$$Z_{ok}^{*}(x) = \sum_{\alpha=1}^{m(x)} \lambda_{\alpha}(x) Z(x_{\alpha}) \tag{3}$$

To obtain an unbiased estimator in ordinary kriging, the following equations must be satisfied:

$$\sum_{\beta=1}^{m(x)} \lambda_{\beta}(x)\gamma(x_{\alpha}, x_{\beta}) - \mu(x) = \gamma(x_{\alpha}, x) \quad \text{where} \quad \alpha = 1, \dots, m(x) \tag{4}$$

$$\text{with} \sum_{\beta=1}^{m(x)} \lambda_{\beta}(x) = 1$$

$Z_{ok}^{*}(x)$ represents the predicted value of the variable Z at point x; $Z(x_{\alpha})$ indicates the known value at point x_{α}; $\lambda_{\alpha}(x)$ denotes the weight affected by the data; $\mu(x)$ is the Lagrange multiplier; $\gamma(x_{\alpha}, x_{\beta})$ refers to the variogram value related to the origin at x_{α} and the endpoint at x_{β}; $\gamma(x_{\alpha}, x)$ is the semivariogram value of the model between the sample location x_{α} and the target location $Z_{ok}^{*}(x)$, and $m(x)$ indicates the count of measurement points utilized in the estimation. $Z_{ok}^{*}(x)$ may involve either point or block kriging. This study employs point kriging, where the estimation occurs at an unknown point (Rouhani, 1996). A comprehensive description of the kriging method is available in the works of (Isaaks and Srivastava, 1989) and (Wackernagel, 2003).

The cross-validation method was used to evaluate the accuracy of ordinary kriging for each variogram model. In this study, cross-validation was conducted by calculating the residual sum of squares (RSS) and the mean squared deviation ratio (MSDR), which satisfy the following equations:

Residual sum of squares (Goovaerts, 1997);

$$RSS = \sum_{i=1}^{n} [\hat{\gamma}(h) - \gamma(h)]^2 \tag{5}$$

$\hat{\gamma}(h)$ and $\gamma(h)$ are the experimental and model variograms, respectively, expressed in Eq. (1) and (2).

The mean squared deviation ratio (Goovaerts, 1997);

$$MSDR = \frac{1}{m} \sum_{i=1}^{m} \frac{[Z(x_i) - Z^{*}(x_i)]^2}{\sigma_k^2(x_i)} \tag{6}$$

$Z(x_i)$ is the observed (actual) value at location i. $Z^{*}(x_i)$ is the estimated kriging value at location i. $\sigma_k^2(x_i)$ is the kriging variance and i is the number of cross-validated data points.

5. Results and Discussion

5.1 Complete Bouguer Anomaly and Regional Anomaly

The results of gravitational acceleration processing in the form of a complete Bouguer anomaly map (CBA) range from 143.77 to 281.43 mGal. The CBA map shown in Fig. 3 indicates that the Tengger volcanic rocks (Tdk) produce high gravity anomaly values in the southern part of the caldera, whereas the young cone complex pyroclastic fall (Cmjp) results in low gravity anomalies in the northern part of the caldera. The CBA map displays a dominant

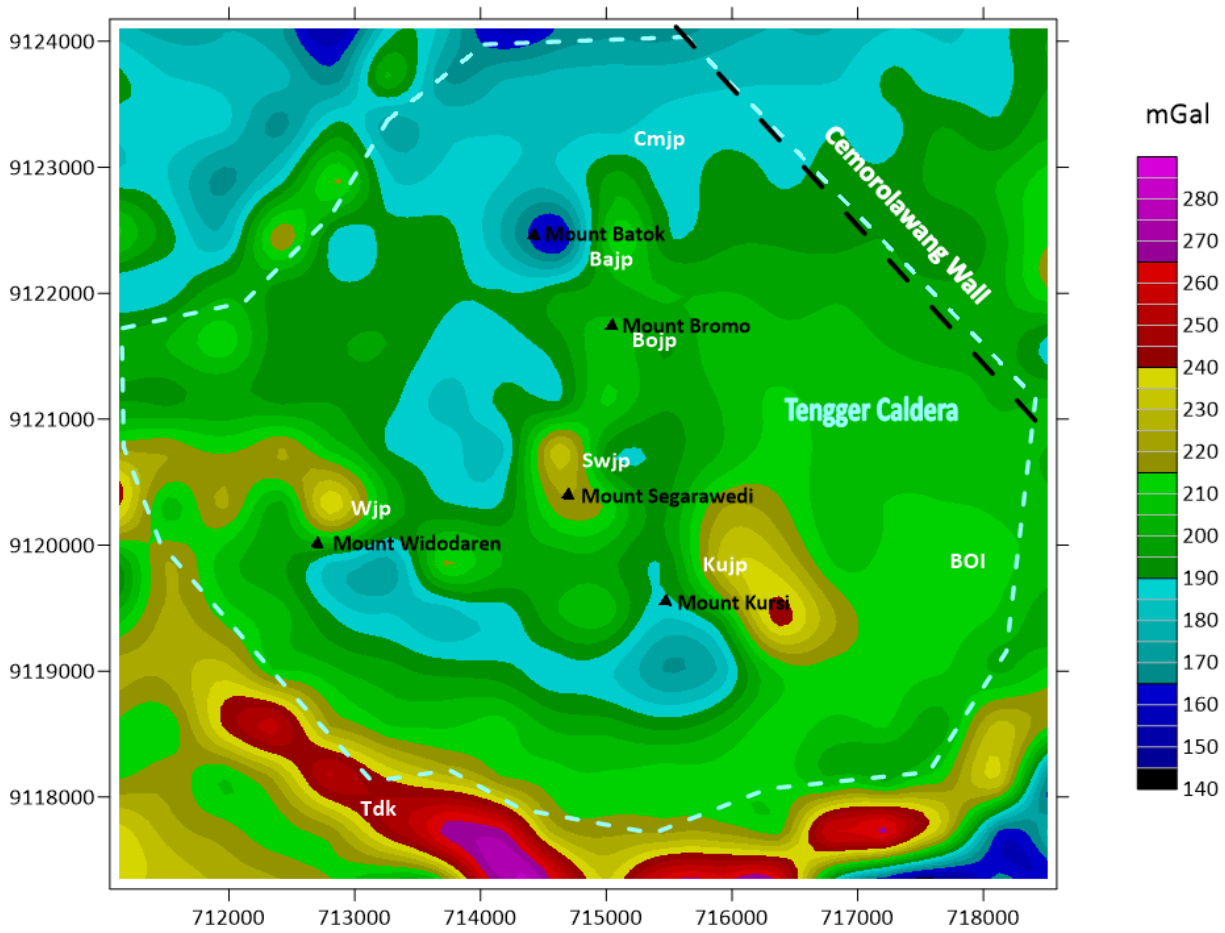

Figure 3. Complete Bouguer anomaly map of the study area. The black dashed line indicates the continuity of the Cemorolawang Wall, whereas the blue dashed line shows the caldera boundary and rock units based on the geological map produced by Mulyadi (1992).

characteristic of a significant gravity anomaly contrast along the caldera wall; however, as shown by the geological map in Fig. 2a, it is not yet capable of representing variations in rock units within the study area. In addition, the CBA map does not indicate the continuity of the Cemorolawang wall in the northeastern part of the caldera.

An elevation leveling process termed planar reduction is performed on the CBA map to project the gravity data from the undulating observation surface onto a flat plane. Standard Bouguer and terrain corrections effectively remove the gravitational effects of surrounding topographic masses, but they do not alter the physical elevation of the observation points; hence, the resulting CBA values remain tied to the irregular drape surface. Treating gravity data from an undulating surface as if it lies on a flat plane during grid-based operations – such as geostatistical kriging and regional-residual separation – introduces severe elevation-induced distortions. To mitigate these artificial mathematical anomalies, the equivalent source technique (Dampney, 1969) is applied as a method for elevation leveling onto a uniform horizontal datum, referred to as the Gridded Horizontal Plane (GHP). It works by mathematically placing an imaginary layer in the form of an equivalent source plane at a certain depth beneath the Earth's surface. The density or strength of these hidden sources is calculated such that their gravitational effect exactly matches the actual raw data measured on the uneven surface. Once the values of these sources are determined, they can be used to recalculate the field values at the selected gridded horizontal plane (GHP) elevation, thus eliminating distortions caused by topographic fluctuations while retaining important signals from deeper geological structures. According to Dampney (1969), aliasing must be prevented by ensuring that the equivalent depth is 2.5 to 6 times the spacing between data points. The spacing between data points was set at 400 m. The lowest and highest elevation measurement points were 1869 and 2980 m, respectively. The equivalent source plane varied between 869 and −531 m, and the gridded horizontal plane was adjusted between 2980 and 4500 m. To determine the most appropriate parameters for the elevation projection, a statistical analysis based on the lowest values of the

residual sum of squares (RSS) and standard deviation (SD) (Cressie, 1985; Isaaks and Srivastava, 1989; Oliver and Webster, 2014) was performed, yielding an optimal equivalent source plane at 0 m and a GHP at 2,980 m (Table 1).

The next step was to separate the anomalies using a moving average filter to produce a regional anomaly, applying the 7 × 7 grid-cell window determined from the spectral analysis described above. The result of the moving average filter was a regional anomaly map (Fig. 4). Regional gravity anomalies are usually caused by anomaly sources

Table 1. The residual sum of squares and standard deviation of the complete Bouguer anomaly (CBA) were calculated for various equivalent source planes and gridded horizontal planes.

Equivalent Source Plane	Residual Sum of Square			Standard Deviation		
	GHP 2980m	GHP 3500m	GHP 4500m	GHP 2980m	GHP 3500m	GHP 4500m
−531 m	1909.95	2394.57	2249.91	4.321	4.653	4.442
0 m	1906.72	2587.87	2399.14	4.162	4.739	4.517
500 m	2851.91	3975.08	3217.50	5.000	5.831	5.207
869 m	5917.77	4573.79	4101.82	6.314	7.120	5.874

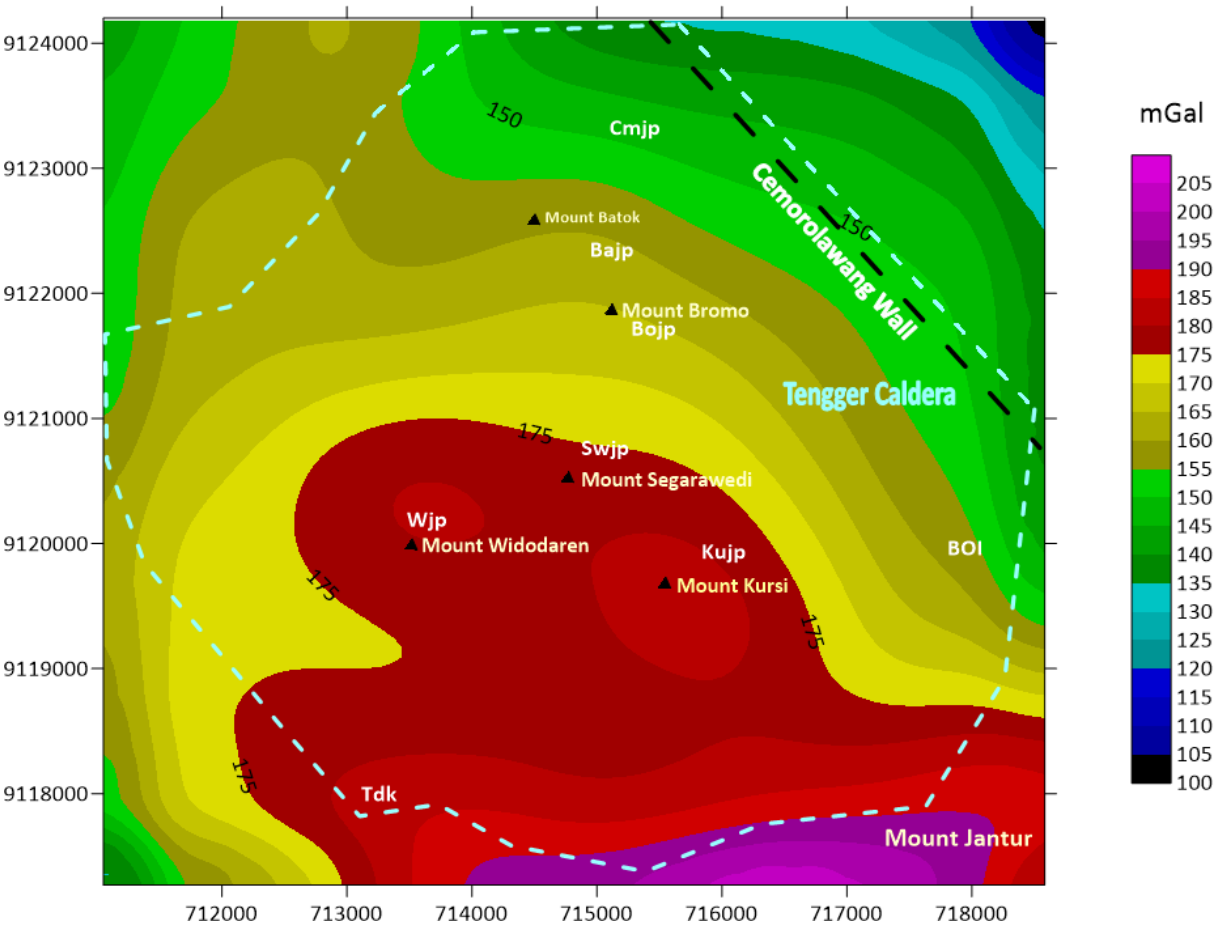

Figure 4. Regional gravity anomaly at an equivalent source depth of 0 m and gridded horizontal plane of 2980 m. The black dashed line represents the lineament of the Cemorolawang Wall. The caldera boundary is indicated by a blue dashed line. The rock units are provided by the geological map by Mulyadi (1992).

located far below the surface. Therefore, in this study, regional gravity anomalies cannot indicate the continuity of the Cemorolawang Wall, as this continuity lies relatively close to the surface. The regional gravity anomalies show the presence of high-density rocks beneath Mount Widodaren, Mount Segarawedi, Mount Kursi, and the southern area of the caldera, which comprises the Tengger volcanic rocks and Mount Jantur. These high-density rocks likely formed from the remnants of volcanic activity that occurred approximately 1,760 years ago after the caldera formed (Zaennudin et al., 1994). The high-density values in the caldera area are probably due to the cooling of the magma body and gas reduction during magma supply periods. This cooling and gas reduction process is a natural consequence of decreasing magma supply over time (Berrino et al., 1992). In the study area, high-density rocks at depths of up to 5 km represent remnants of magma pipes or intrusions (sills/dikes) that solidified beneath these mountains (Ibrahim et al., 2025).

In contrast, the Mount Bromo area has a lower anomaly (155-175 mGal) caused by volcanic activity, supported by the presence of a magma chamber at depths of 2.5-12.5 km (Wuryani et al., 2014; Zaennudin et al., 2012). This magmatic activity results in lower density values at Mount Bromo and its surroundings compared with other mountains that no longer exhibit volcanic activity. Meanwhile, a lower anomaly is also found at Mount Batok, but volcanic activity in that area ceased approximately 0.36 ka ago (Zaennudin et al., 1994); therefore, the rocks composing Mount Batok are relatively younger, which causes the regional anomaly values to be lower than the anomaly values at Mount Widodaren, Mount Segarawedi, and Mount Kursi.

5.2 Geostatistical Analysis and Residual Gravity Anomaly

Residual gravity anomalies were calculated by subtracting regional gravity anomalies from Bouguer gravity anomalies. These residual gravity anomalies are influenced by the gravity of structures in the middle and upper crust. The residual anomaly map (Fig. 5) does not clearly define features, such as the Tengger Caldera boundary, continuity of the Cemorolawang Wall, and rock units within the caldera. Therefore, geostatistical analysis was performed on the residual gravity anomalies to clarify these features.

The initial step in the geostatistical analysis was to examine the histogram of the residual gravity anomaly. Because the initial histogram of the residual gravity anomaly did not closely follow a normal distribution with a skewness of 0.663, a quadratic transformation was applied to make it approach a normal distribution, thereby reducing the estimation errors (Oliver and Webster, 2014). After the quadratic transformation, the skewness of the histogram became 0.624. The variance and standard deviation were reduced to 220.776 and 14.858, respectively (Table 2).

After generating a histogram that closely approaches a normal distribution, the next step is to create an experimental variogram based on Eq. (1). At this stage, the data are sorted by distance with a lag distance (h) of 227 m. The calculation of the experimental variogram involves 15 lags, a search radius of 5110 m, and a minimum of eight to a maximum of 16 data points to ensure adequate spatial coverage across the entire 7 × 8 km caldera area. This approach ensures the preservation of spatial correlation among data points, allowing for reliable semivariogram estimation and facilitating accurate spatial predictions throughout the study area (Zimmerman et al., 1999). Table 3 presents the results of the experimental variogram calculation, which were used to produce the experimental variogram graph in Fig. 6.

The next stage in the geostatistical analysis is to determine the most suitable variogram model. The least-squares method is used to determine this model, which shows how well the model fits the experimental variogram

Table 2. Descriptive statistics of the residual gravity anomalies.

Statistics	No Transformation	Quadratic Transformation
Variance	221.088	220.776
Standard Deviation	14.869	14.858
Coefficient of skewness	0.663	0.624

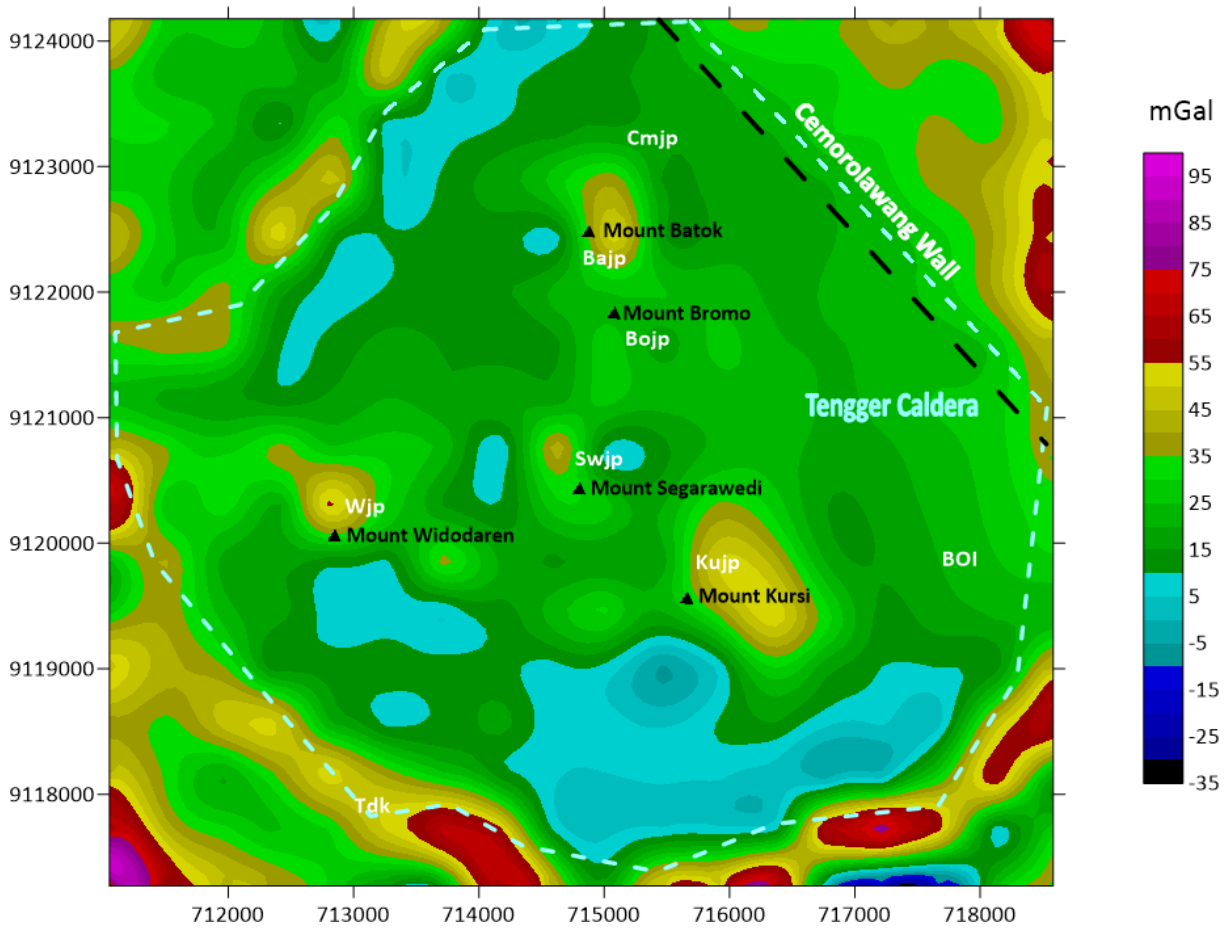

Figure 5. Map of the residual gravity anomaly in the study area. The black and blue dashed lines indicate the continuity of the Cemorolawang Wall and the caldera boundary, respectively. The geological map was based on a study by Mulyadi (1992), showing the rock units present in the study area.

(Cressie, 1985). Each variogram model produces geostatistical parameter values, such as range, nugget, and sill, based on Eq. (2). A cross-validation technique is applied to each variogram model to validate the results of ordinary kriging . This method involves removing each of the N data points from the dataset and using kriging based on the variogram model to predict its value (Deutsch, 2002; Isaaks and Srivastava, 1989). The best cross-validation results are those with the smallest residual sum of squares (RSS) and a mean square deviation ratio (MSDR), which is calculated by dividing the RMS value by the kriging variance. Although RMS values indicate optimal kriging results, with lower RMS values being preferable, RMS alone is insufficient to identify the most appropriate variogram model; therefore, the MSDR value is needed to support it. For kriging purposes, the best results are achieved when the MSDR value of the variogram model is close to 1 (Oliver and Webster, 2014). Diagnostic results from this study show that the Gaussian variogram model is the most suitable for gravity data in the study area, as it has the smallest RSS value and an MSDR close to 1 compared to the spherical and exponential models (Table 4). However, the Gaussian variogram model has a larger nugget value than the other models. In volcanic areas, a large nugget effect reflects highly complex subsurface geological conditions, such as sharp density contrasts over short distances and surface variations that occur on scales smaller than the spacing between observations, resulting in the variogram being unable to map the pattern continuously.

Figures 7a, 7c, and 7e show the overlap of the experimental variogram graph with the spherical, exponential, and Gaussian variogram models, respectively. Qualitatively, the fit of the three variogram model graphs to the experimental variogram appears good, making it difficult to determine which variogram model is the best for interpretation. Figure 7f shows that the Gaussian model can reduce the "bull's-eye" effect seen in the spherical (Fig. 7b) or exponential (Fig. 7d) models, resulting in a sharper and more continuous density gradient at the boundary between the Tengger Caldera and the Cemorolawang Wall.

Table 3. Experimental variogram values of the residual gravity anomalies.

Lag Distance	Semivariance	Experimental Variogram
435.28	128.53	577
615.63	153.35	544
870.59	183.39	542
973.37	167.77	1022
1299.59	184.18	1463
1507.44	182.79	1378
1756.88	183.36	914
1887.76	191.94	1704
2194.02	184.61	2043
2382.11	194.01	1138
2617.99	187.66	2236
2838.41	193.08	1700
3097.38	192.65	2311
3303.50	200.28	1224

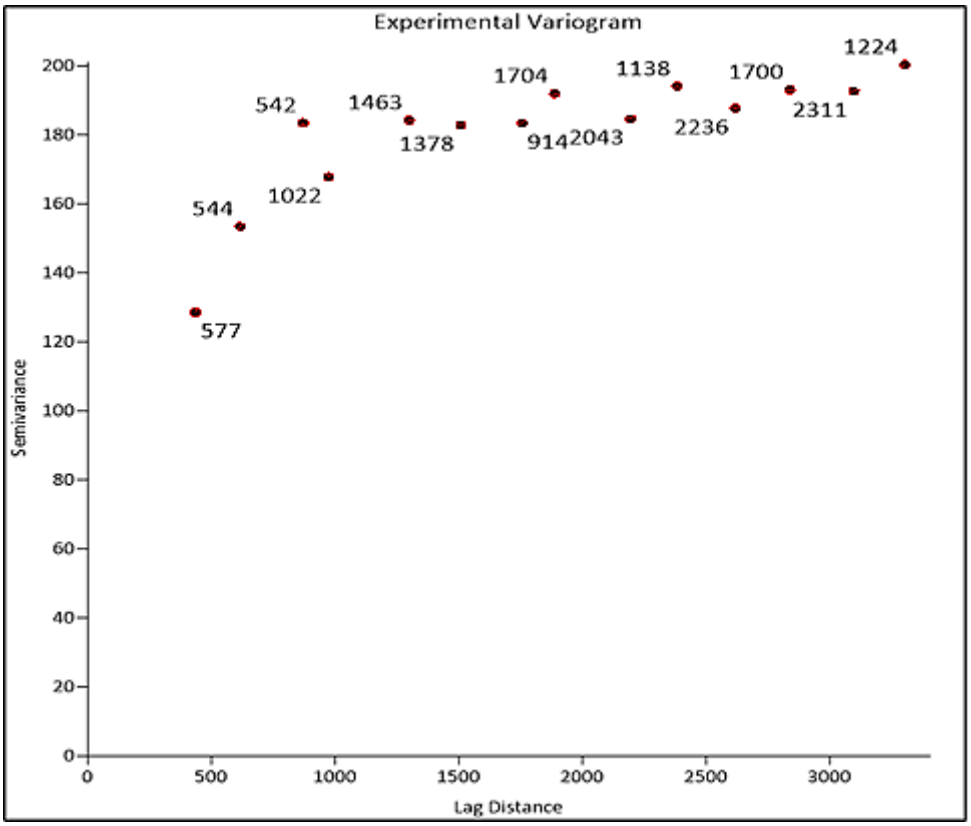

Figure 6. Experimental variogram for residual gravity anomalies.

Table 4. Model parameters and diagnostics of the variogram model fitted to the experimental variogram.

Model	Estimates of parameters			Diagnostics			
	Sill	Range	Nugget	Kriging variance	RSS[a]	RMS[b]	MSDR[c]
Spherical	138	2200	50	159.86	15915.89	159.16	0.996
Exponential	140	990	50	152.97	15224.93	152.25	0.995
Gaussian	93	990	95	127.16	12686.58	126.87	0.998

[a]RSS is residual sum of squares
[b]RMS is residual mean square
[c]MSDR is mean squared deviation ratio

5.3 Volcano-Tectonic Implications of the Variogram Signature

A comparative diagnostic review of the geostatistical modeling indicates that the Gaussian variogram model superiorly resolves the spatial architecture of the Bromo-Tengger gravity field over the spherical and exponential formulations. The Gaussian model minimizes spatial estimation errors, yielding the lowest Kriging variance 127.16, a highly reduced Residual Sum of Squares (RSS = 12686.58), and a minimized Root Mean Square (RMS) error of 126.87. Most notably, its Mean Square Deviation Ratio (MSDR = 0.998) demonstrates an exceptional compliance with the theoretical ideal of 1.0, validating the integrity of the computed kriging variance.

Despite this robust statistical fit, the model exhibited a prominent nugget effect ($C_0 = 95$) that accounted for approximately 50.5% of the total sill variance ($C_0 + C = 188$). Within the framework of high-precision satellite gravity data, this high nugget value cannot be dismissed as random instrumental noise. Instead, it reflects the severe subgrid lithological and structural heterogeneities characteristic of an active caldera system. The shallow subsurface of the Bromo-Tengger complex is intensely chaotic, defined by intercalated sequences of low-density unconsolidated tephra and pyroclastic surge deposits that alternate abruptly with high-density, consolidated basaltic-andesitic lava flows (Zaennudin, 2011; Zaennudin et al., 1994). Furthermore, the presence of localized dense rocks, shallow subvolcanic sills, and intense fracture network zones introduces high-frequency density contrasts that occur at wavelengths far shorter than the observation grid spacing. Statistically, these unresolvable microfeatures manifest as a non-zero intercept at the variogram origin. This interpretation warrants careful consideration because the short-wavelength components of the GGMplus dataset are partially based on topographic forward modeling rather than direct ground measurements. Consequently, some of the nugget variance may arise from uncertainties inherent in the modeling process at short wavelengths, rather than exclusively reflecting genuine sub-grid geological heterogeneity.

Conversely, the modeled spatial range (990 m) defines the deterministic threshold of the spatial continuum. Within this ~1 km boundary, the gravity field possesses a smooth, continuous spatial correlation that successfully captures the macro-to-meso-scale volcano-tectonic architecture of the region. This spatial range aligns structurally with the regional fault systems governing the East Java microcontinent derivatives and the broader geometry of the caldera collapse floor. However, these structural interpretations must be strictly contextualized within the resolution boundaries of the GGMplus dataset. Featuring a nominal spatial resolution of ~200 m (~10 arc-seconds), the high-frequency components of GGMplus are heavily constrained by forward-modeling of topographic masses. Consequently, localized subsurface density variations that lack an explicit surface topographic expression, such as blind faults or deep-seated magmatic pathways, approach the limits of detectability. While the optimized Gaussian model excels at delineating the continuous regional-residual structural framework of the Bromo-Tengger complex down to the basement depth, shifting their signatures into the unresolved nugget component and highlighting the ongoing necessity for complementary ground-based gravity surveys.

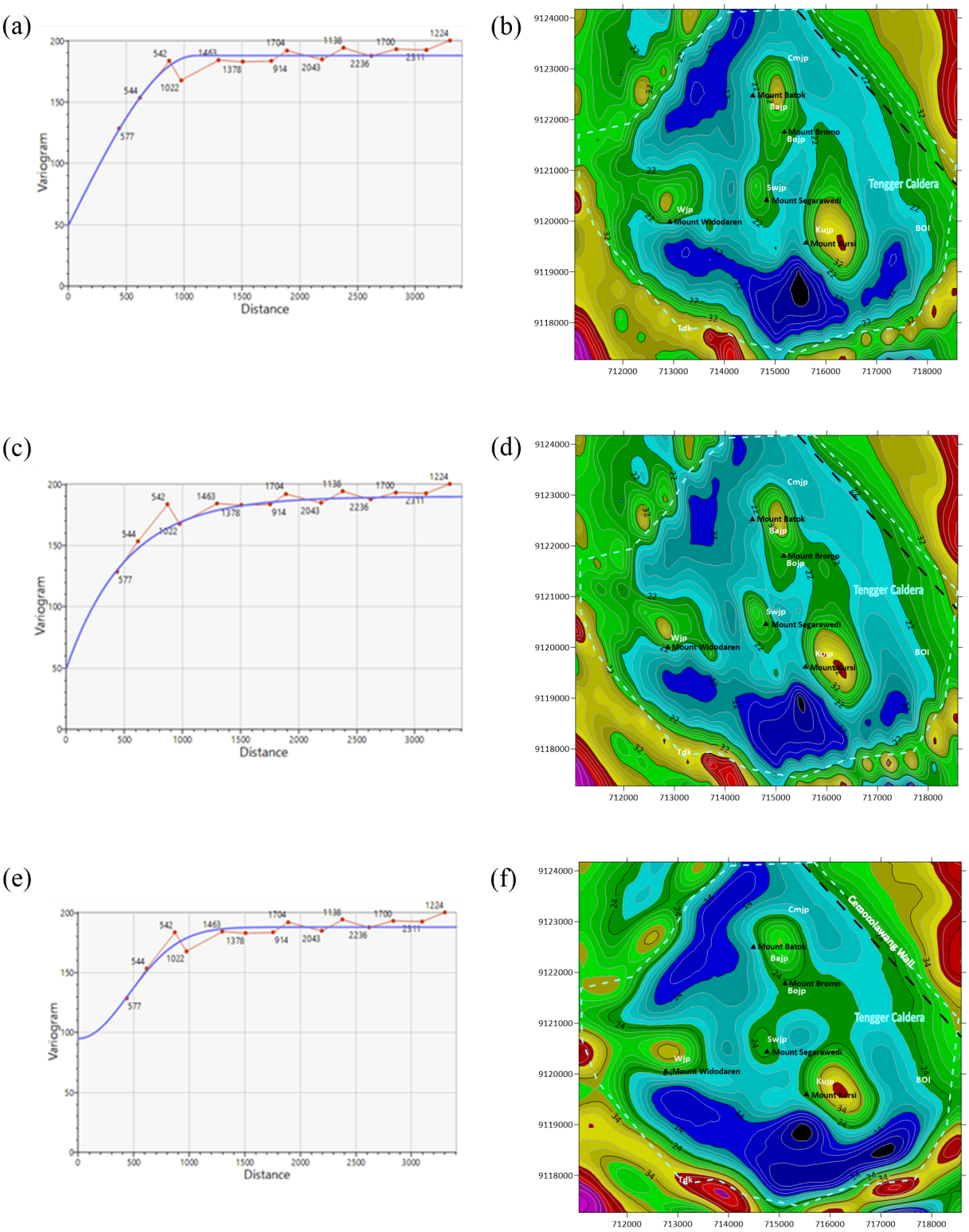

Figure 7. The red graph shows the experimental variogram, and the blue graph illustrates the variogram model. (a) and (b) show the variogram and residual gravity anomaly for the spherical model; (c) and (d) show the variogram and residual gravity anomaly for the exponential model; (e) and (f) show the variogram and residual gravity anomaly for the Gaussian model, respectively. The continuity of the Cemorolawang Wall is indicated by the black dashed line, and the caldera boundary is indicated by the blue dashed line. The rock units were obtained from Mulyadi's (1992) geological map.

5.4 Structural Boundary Analysis Using Total Horizontal Derivative (THD)

The total horizontal derivative (THD) measures the rate at which the gravity field changes laterally. Because the sharpest lateral changes in gravity occur immediately above the edges of underground density contrasts, the highest THD values form ridges that align closely with the boundaries of these density-contrast bodies. This makes THD a reliable and widely used method for precisely mapping faults, lithological contacts, and other structural boundaries directly from potential-field data (Blakely, 1995; Grauch and Cordell, 1987). The Total Horizontal Derivative (THD) map presented in Fig. 8 provides robust spatial confirmation of the structural boundaries within the Bromo-Tengger Volcanic Complex. This boundary analysis was executed using gravity data to sharpen and clarify the structural limits previously identified in the residual anomaly map. While the residual map outlines the broad distribution of mass deficits and excesses, the THD technique is highly sensitive to sharp lateral changes in rock density. This allows for a clear and objective mapping of subsurface structural margins, where the highest derivative values – represented by the prominent red to magenta colorations – signify the exact location of geological boundaries and outline the main physiographic rim of the caldera depression. The enhanced THD map successfully isolates and resolves the complex structural architecture of the area into three primary components (Fig. 8):

1) Inner caldera boundary: At the center of the survey area, corresponding directly to the central low-density residual basin observed in the residual anomaly map, the THD analysis successfully delineates a well-defined, closed circular high-derivative anomaly. This continuous circular ring configuration indicates a sharp, near-vertical lateral density contrast at depth, which is interpreted as the subsurface expression of the inner caldera wall or its associated ring-fault system, isolating the highly collapsed central volcanic depression.
2) Outer arcuate structure: Beyond this central structure, a massive and distinct arcuate (semi-circular) high-THD trend is mapped across the southern to southeastern sectors. This feature functions as an outer arcuate structure that effectively constrains spatial limits and defines the structural boundary of the outer caldera rim. The pronounced spikes in the horizontal gradient along these boundary zones occur because of the sharp density contrast between the high-density rock formations on the outer side (outer flank) and the lower-density volcaniclastic materials within the caldera depression, which is independently confirmed by the low-anomaly zone on the residual anomaly map.
3) Structural lineaments and magmatic pathways: In addition to the primary caldera ring, the THD map successfully identified localized high-gradient structural lineaments distributed around the complex. The presence of these features indicates that the overall structural layout of the Tengger Caldera was heavily influenced by pre-existing fault networks and density contact boundaries. These tectonic elements not only defined the final structural architecture of the caldera but also provided crucial subsurface permeability pathways. These localized networks facilitated post-caldera magmatic migration, which subsequently supported the volcanic plumbing system and the growth of active subsequent cones, such as Mt. Bromo.

By converting broad gravity variations into sharp and well-defined structural lines, this boundary analysis provides robust geophysical constraints on the complex geometry of the caldera. This moves beyond generalized anomaly interpretations, delivering a much clearer, data-supported delineation of the structural margins and evolutionary pathways of the volcanic complex.

5.5 Subsurface Interpretation

Residual gravity anomalies are used to interpret the sources of anomalies that are relatively close to the surface; thus, geological features appear more clearly than on complete Bouguer and regional gravity anomaly maps. The advantage of the residual gravity map shown in Fig. 9a is that it can clearly describe the boundaries of the Tengger Caldera area and the Cemorolawang Wall, as indicated by the differing gradients that reflect variations in rock density compared with previous maps by Maryanto et al. (2017) and Ibrahim et al. (2025). The structural boundary forming the Cemorolawang Wall is believed to have been formed by major NW-SE trending faults within the study area. These faults are likely associated with the predominantly NW-SE continuities seen on the DEM map, as shown in Fig. 2b. These continuities are thought to extend beyond the study area and are controlled by NW-SE trending strike-slip faults (Solikhin et al., 2012). The faults in the study area are manifestations of N-S trending tectonic stress, the pattern of which has remained stable since the Eocene but continues to actively shape the

caldera's morphology until today (Marliyani et al., 2020). The continuity of the fault forming the Cemorolawang Wall disappears near the Tengger volcanic rocks. The fault is believed to continue beneath the Tengger Caldera and contribute to the formation of the fault system within the caldera. This residual gravity anomaly map not only sharply defines the shape of low anomalies but also reveals new geological insights about the study area. This study shows a direct spatial correlation between gravity anomalies and each volcanic cone within the Tengger Caldera, namely, the pyroclastic deposits from Mount Batok (Bajp), Mount Segarawedi (Swjp), Mount Widodaren (Wjp), and Mount Kursi (Kujp). However, this residual anomaly map has a drawback, namely, it cannot map the Bromo basal lava flows (BOI-1 and BOI-2) located on the northwestern and eastern parts of the caldera. This may be because the basal lava is a surface deposit that cannot be detected by residual anomalies, which can only capture sources at greater depths. The interpretation of these features provides important insights into the tectonic and volcanic evolution of the study area.

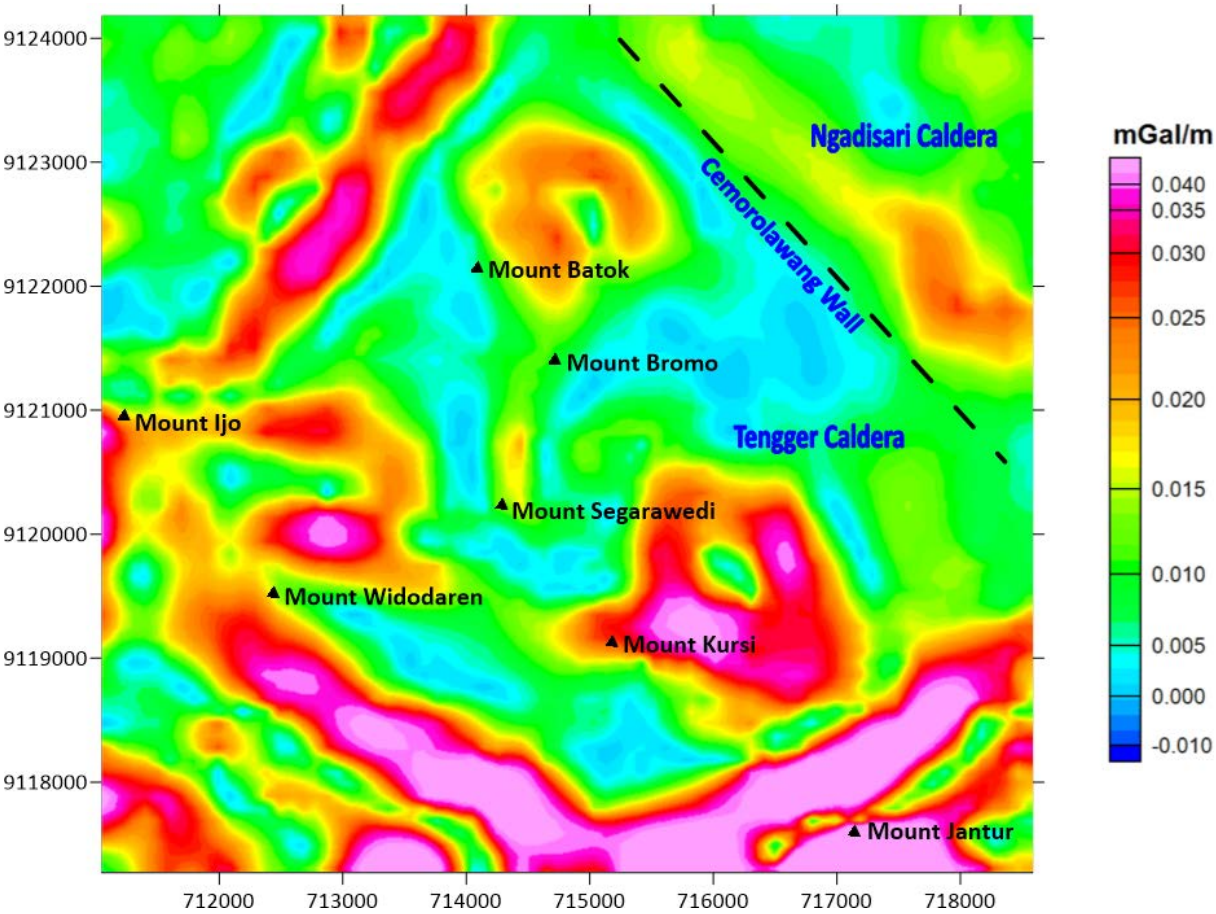

Figure 8. Total horizontal derivative (THD) map of the study area derived from the residual gravity anomaly. Prominent high-gradient peaks (indicated by the red-to-magenta color spectrum) delineate major subsurface structural contacts and density boundaries, outlining a well-defined closed circular inner caldera wall at the center and a massive outer arcuate structure along the southern and southeastern margins of the Tengger Caldera depression.

The residual gravity anomaly cross-section in Fig. 9b shows low anomaly values ranging from 6 to 14 mGal at distances between 2.5 and 3.2 km. This anomaly indicates the presence of a significant volume of low-density volcanic material in the form of unconsolidated pyroclastic deposits and fallout (Cmjp), filling the caldera basin as a result of post-eruption collapse (Miller et al., 2022). The maximum residual gravity anomaly value, exceeding 40 mGal, is located at 0-0.5 km in the southwestern part of the caldera and at 9.5-10 km in the northeastern part, which consists of layered igneous rocks forming the Tengger volcanic rocks (Tdk). Meanwhile, between 4.5 and 6.5 km, the rocks forming Mount Segarawedi and Bromo are dominated by anomalous values ranging from 22 to 32 mGal.

To quantitatively estimate the subsurface geometry and delineate the depth of the caldera basement, 2D gravity inversion modeling was executed along the A-B profile line. The application of a 2D inversion scheme is geologically justified by the dominant regional structural lineaments and fault systems within the Bromo-Tengger complex, which run predominantly perpendicular to the profile direction, thereby satisfying the infinite-strike assumption for this localized section. This structural setup builds upon the foundational regional tectonic framework of Indonesia established by Hamilton (1979) and the volcano-tectonic insights of Busby and Bassett (2007), which link regional tectonic stress, active fault systems, and basin subsidence to the spatial distribution of volcanic complexes. To mitigate the inherent non-uniqueness and ambiguity characteristic of potential field data, a smoothness-constrained inversion approach was adopted to yield a mathematically stable subsurface density distribution. The processing methodology incorporates field gravity survey principles and gravity gradient fault mapping originally pioneered by Edge and Laby (1931), utilizing a standard historical crustal reduction density of ~2.67 g/cm^3 for topographic corrections. The inversion process was strictly regularized using physical density boundaries derived from a comprehensive synthesis of local volcanostratigraphy and regional analog gravity models, including works by Untung and Hasegawa (1982), Cas and Wright (1996), Zaennudin et al. (1994), Smyth et al. (2008), Setiadi (2012) and Pratiwi et al. (2026). The inversion converged after ten iterations, meeting the modeling software's default convergence criterion of a change of less than 0.1% between successive iterations. The calculated gravity response (Fig. 9c) effectively captures the smooth regional-scale trend of the observed anomaly along the A-B profile. However, the notable short-wavelength variations observed in the data were not reproduced by the smoothed 2D model. This discrepancy aligns with the pronounced nugget effect described in previous section, indicating sub-grid heterogeneity that exceeds the resolution capabilities of a single 2D profile inversion.

The resulting preliminary inversion model, illustrated in Fig. 9d, reveals a subsurface density spectrum ranging from 1.9 to 2.8 g/cm^3, representing a transition from shallow, loose pyroclastic infill to a rigid basement composed of basaltic andesite bedrock or older igneous successions (Santamaria and Suwarti, 1992; Satyana, 2005; Smyth et al., 2005, 2008; Untung and Hasegawa, 1982). Based on the inverted density distributions, the subsurface architecture of the Tengger caldera was parameterized into three distinct layers. The uppermost layer, characterized by a density range of 1.9 to 2.0 g/cm^3, corresponds to the youngest eruptive products from the recent volcanic activity of Mount Batok and Mount Bromo (Gottschammer and Surono, 2000; Zaennudin, 2011). This surficial unit lithologically comprises unconsolidated volcanic ash, volcanic sand, lapilli, and volcanic bombs, where the remarkably low bulk density is directly supported by physical volcanology core texts like Cas and Wright (1996), which establish density constraints for loose pyroclastics and tephra between 1.4 and 2.2 g/cm^3. This is further supported by Gunawan et al. (2021), who inferred low densities of approximately 1.60 to 2.10 g/cm^3 for shallow pyroclastic and scoria flows based on a structural geochemical context. Directly beneath this surficial pyroclastic layer lies an intermediate zone with a density range of 2.1 to 2.5 g/cm^3, representing an accumulation of older eruptive sequences that have undergone progressive mechanical compaction. This layer consists of alternating successions of andesitic lava flows, volcanic breccias, and dense tuffs, frequently hosting distinct subvolcanic conduits or lava plugs (Gottschammer and Surono, 2000). The density constraints and magmatic structural boundaries of this intermediate zone align with recent local modeling in East Java by Pratiwi et al. (2026), who defined volcanic and intrusive layers ranging from 2.3 to over 2.6 g/cm^3.

At an approximate depth of 4.5 km, a prominent structural transition was identified, where density values increased to 2.6-2.7 g/cm^3, marking the boundary toward highly compact ancient volcanic units and Tertiary sedimentary rocks (Smyth et al., 2008). This deep architecture relies on the primary reference densities for Java crustal rocks established by Untung and Hasegawa (1982), which typically range from 2.50 to 2.70 g/cm^3. The maximum density values within this deeper realm reach up to 2.8 g/cm^3, defining the crystalline or rigid structural basement of the caldera itself. This characterization is supported by Smyth et al. (2005, 2008), who inferred a basement composition of approximately 2.7+ g/cm^3 beneath East Java to support modern volcanic evolution and basement-characterization models. The presence of deep marine sediment intercalations within this basement layer is a characteristic regional geological feature of East Java that structurally underpins the contemporary active volcanic complexes (Lunt, 2019). However, it must be emphasized that the density distribution presented in this study serves as a preliminary inversion model. Owing to the mathematical limitations regarding depth resolution and non-uniqueness inherent to gravity field modeling, further validation using independent, high-resolution geophysical datasets – such as seismic reflection or refraction profiles and magnetotelluric (MT) soundings – alongside deep structural or borehole data remains essential in future studies to fully substantiate and refine these initial lithodensity boundaries.

The caldera basement was visible at a depth of 4.5 km with a density of 2.8 g/cm^3. This depth represents the boundary between the rigid basaltic-andesitic basement rock (Satyana, 2005) and the overlying volcanic material.

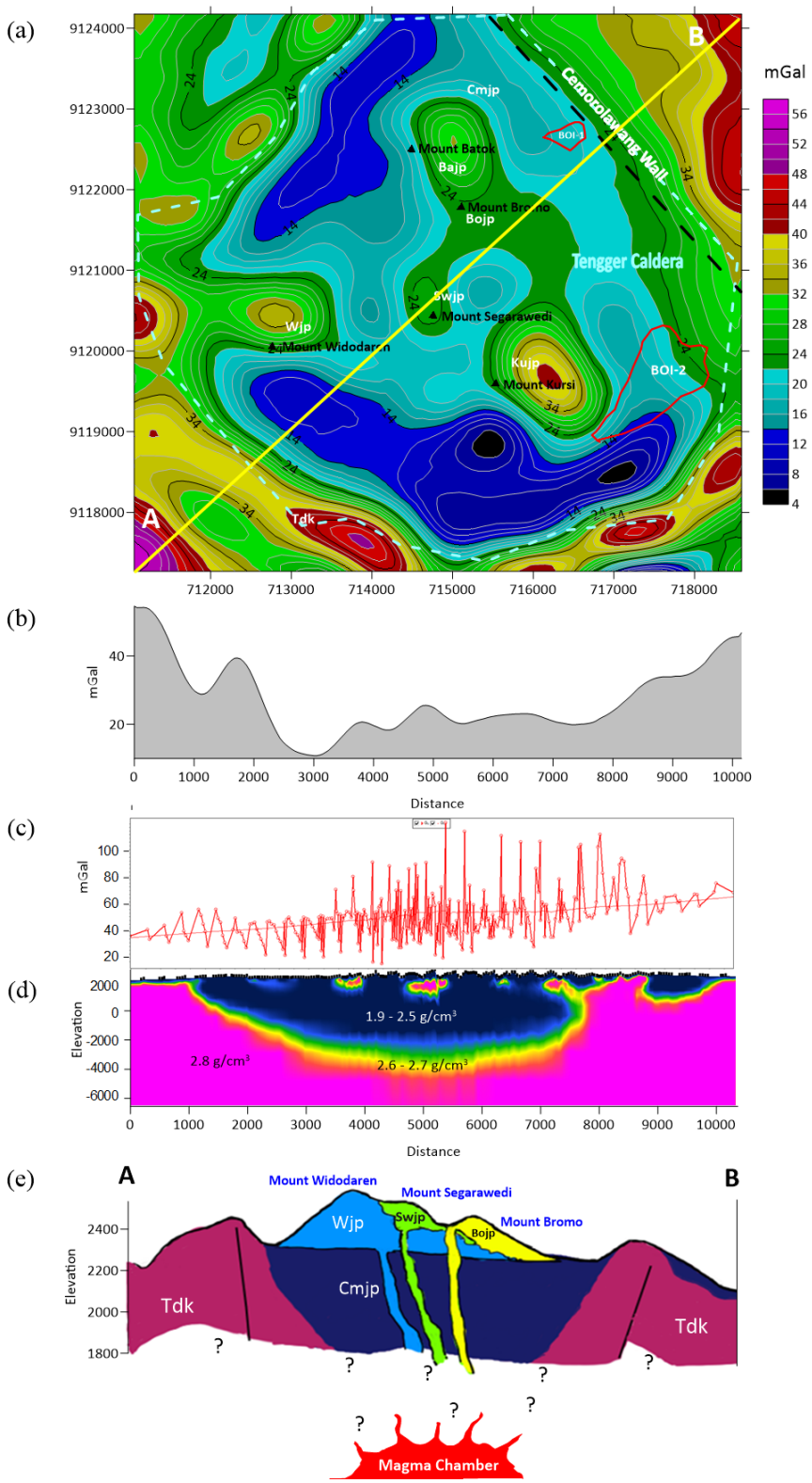

Figure 9. (a) Residual gravity anomaly for the Gaussian variogram model, showing the A-B cross-section line; (b) residual gravity anomaly cross-section based on the A-B section; (c) 2D gravity profile of the study area. The line with circular markers (Go) corresponds to the observed gravity data, whereas the smooth solid line (Gc) represents the calculated gravity response based on the final subsurface density model; (d) preliminary inversion modeling estimating the caldera base at a depth of approximately 4.5 km; and (e) initial subsurface interpretation of the Bromo-Tengger volcanic complex, which includes pyroclastic fall deposits filling the Tengger caldera (Cmjp), the Tengger volcanic rocks (Tdk), pyroclastic fall from Mount Widodaren (Wjp), pyroclastic fall from Mount Segarawedi (Swjp), pyroclastic fall from Mount Bromo (Bojp), and pyroclastic fall from Mount Batok (Bajp).

The depth of the caldera basement resulting from the inversion model closely matches the depth of the basement studied by Smyth et al. (2005, 2008), who stated that the high density at depths of 5 to 10 km reflects continental basement rock, which is part of the East Java micro-continental fragment accreted from the Gondwana (Australia) margin during the Cretaceous period and consists of strongly consolidated igneous rocks or possibly high-grade metamorphic rocks. Hall, (2002) also stated that the bedrock characteristics beneath the Bromo-Tengger complex are regional manifestations of the complex tectonic evolution of Southeast Asia, where the presence of a high-density mass at a depth of approximately 5.5 km reflects the East Java microcontinental fragment, which has a higher density than oceanic crust. This condition is reinforced by the long-standing subduction process along the eastern Indonesian volcanic arc, which has caused the basement rock to experience extreme consolidation and massive structural compaction (Hamilton, 1979), thereby creating a rigid crystalline foundation for the overlying magmatic system. According to Ibrahim et al. (2025), depths of more than 5-20 km indicate the physical manifestation of the magma reservoir and its connection with the main magma chamber, which is aligned with the N-S fault orientation. However, to further ensure the depth of the caldera basement, additional research using other geophysical methods should be conducted.

A cross-section was constructed using the inversion results and rock unit correlations to depict the distribution of rock units along Line A-B (Fig. 9e). According to Zaennudin et al. (1994), the formation of the series of mountains – namely, Mount Widodaren (Wjp), Mount Segarawedi (Swjp), Mount Kursi (Kujp), and Mount Batok (Bajp) – began 1,810 years ago. Meanwhile, Mount Bromo (Bojp), formed 360 years ago, is the only active volcano in the Tengger Caldera today. Based on volcanostratigraphy and petrogenesis studies conducted by Abrory (2019), the rock units, if arranged from oldest to youngest, are Tdk, Wjp, Kujp, Swjp, Bajp, and Bojp. The sequence of these rock units is influenced by certain linear features that align with the orientation of regional stress. This proves that fractures at the base of the caldera are controlled by larger tectonic forces, not just local volcanic processes. According to Marliyani et al. (2020), tectonic activity in the study area is influenced by the Rembang-Madura-Kangean-Sakala Fault Zone (RMKS), which then creates an extensional setting or areas of crustal weakening, thus forming pyroclastic cones inside the Tengger Caldera.

The integrated analysis of these features significantly enhances the understanding of subsurface dynamics in the study area and its surroundings, thereby providing valuable contributions to geoscientific exploration, disaster mitigation, and natural resource estimation in the Bromo-Tengger volcanic complex.

6. Conclusion

Geostatistical analysis, particularly the use of the Gaussian variogram model, has proven to be highly effective in improving the accuracy of gravity data interpretation in the Bromo-Tengger volcanic complex. This model produced an MSDR value of 0.998, indicating a high level of precision in mapping subsurface conditions compared to other variogram models. This study succeeded in reducing estimation errors and generating a residual anomaly map that provides a sharper and more continuous geological image using the ordinary kriging method. The results of this research clearly identify the boundaries of the Tengger Caldera and the Cemorolawang Wall's linearity, which is controlled by a NW-SE trending strike-slip fault system. The residual anomaly map reveals significant density contrasts between the caldera volcanic rocks (Tdk), which have high anomaly values, and the pyroclastic deposits (Cmjp), which fill the caldera floor with lower anomaly values. Additionally, a strong spatial correlation exists between gravity anomalies and each volcanic cone within the caldera. Preliminary inversion modeling indicates that the caldera basement rocks are located at a depth of approximately 4.5 km with a high density (2.8 g/cm^3). Overall, the integration of these data provides an in-depth understanding of the subsurface structure and distribution of rock units, ranging from the oldest caldera wall formation to the youngest volcanic cone of Mount Bromo. This research also offers a valuable reference for future geoscientific exploration and sustainable natural resource management in the study area.

Data availability statement. Data used in this paper can be downloaded at: https://geodesy.curtin.edu.au/research/resolution/ for gravity acceleration data and at https://earthexplorer.usgs.gov/ for elevation data with coordinates from −7.9500 to −7.6000 Latitude and 112.9000 to 113.5500 Longitude.

AI declaration. The preparation of this manuscript utilized Paperpal (Cactus Communications) as a writing assistant to enhance the quality of grammar and technical flow. All suggestions provided by the software were manually reviewed and validated by the authors. The authors bear full responsibility for the scientific integrity and content of this manuscript.

Acknowledgements. We are grateful to the reviewers and editors for their valuable comments that have helped to improve this manuscript. We also thank our colleagues from Gadjah Mada University and the Sepuluh Nopember Institute of Technology for their assistance.

References

Abrory, A. N. (2019). Vulkanostratigrafi dan Petrogenesis Gunung Bromo dan Sekitarnya, Kabupaten Probolinggo, Provinsi Jawa Timur. Institut Teknologi Bandung.

Belkhiri, L., A.Tiri and L.Mouni (2020). Spatial Distribution of the Groundwater Quality Using Kriging and Co-kriging Interpolations, Groundwater for Sustainable Development, 11, 100473, doi:10.1016/j.gsd.2020.100473.

Bellotti, F., L. Capra, D. Sarocchi and M. D'Antonio (2010). Geostatistics and multivariate analysis as a tool to characterize volcaniclastic deposits: Application to Nevado de Toluca volcano, Mexico, J. Volcanol. Geoth. Res., 191, 1-2, 117-128, doi:10.1016/j.jvolgeores.2010.01.005.

Berrino, G., H. Rymer, G. C. Brown and G. Corrado (1992). Gravity-height correlations for unrest at calderas, J. Volcanol. Geoth. Res., 53, 1-4, 11-26, doi:10.1016/0377-0273(92)90071-K.

Blakely, R. J. (1995). Potential Theory in Gravity and Magnetic Applications (1st ed.). Cambridge University Press, doi:10.1017/CBO9780511549816.

Bohling, G. (2007). Introduction to Geostatistics and Variogram Analysis, Kansas Geological Survey, https://www.kgs.ku.edu/Publications/OFR/2007/KGSOFR2007-26.pdf.

Busby, C. J. and K. N.Bassett (2007). Volcanic facies architecture of an intra-arc strike-slip basin, Santa Rita Mountains, Southern Arizona, Bull. Volcanol., 70, 1, 85-103, doi:10.1007/s00445-007-0122-9.

Buyung, N., E. Mimanda and A. Susilo (1994). Peta Anomali Bouguer, Jawa; Lembar Malang 1608-1 [Map]. Pusat Penelitian dan Pengembangan Geologi.

Cas, R. A. F. and J. V. Wright (1996). Volcanic successions, modern and ancient: A geological approach to processes, products, and successions. Chapman & Hall.

Cressie, N. (1985). Fitting variogram models by weighted least squares. Journal of the International Association for Math, Geol., 17, 563-586, doi:10.1007/BF01032109.

Dampney, C. N. G. (1969). The Equivalent Source Technique, Geophys., 34, 1, 39-53, doi:10.1190/1.1439996.

Deutsch, C. V. (2002). Geostatistical reservoir modeling, Oxford University Press.

Edge, A. B. B. and T. H. Laby (Eds.) (1931). The Principles & practice of geophysical prospecting: Being the report of the imperial geophysical experimental survey, Univ. Press.

Giustini, F., G. Ciotoli, A. Rinaldini, L. Ruggiero and M. Voltaggio (2019). Mapping the geogenic radon potential and radon risk by using Empirical Bayesian Kriging regression: A case study from a volcanic area of central Italy, Sci. Tot. Environ., 661, 449-464, doi:10.1016/j.scitotenv.2019.01.146.

Goovaerts, P. (1997). Geostatistics for Natural Resources Evaluation. Oxford University PressNew York, NY, doi:10.1093/oso/9780195115383.001.0001.

Gottschammer, E. and I. Surono (2000). Locating tremor and shock sources recorded at Bromo Volcano, J. Volcanol. Geoth. Res., 101, 199-209, https://ncedc.org/ftp/outgoing/peggy/gottschammer.pdf.

Grauch, V. J. S. and L. Cordell (1987). Limitations of determining density or magnetic boundaries from the horizontal gradient of gravity or pseudogravity data, Geophys., 52, 1, 118-121, doi:10.1190/1.1442236.

Gumiaux, C., D. Gapais and J. P. Brun (2003). Geostatistics applied to best-fit interpolation of orientation data. Tectonophysics, 376, 3-4, 241-259, doi:10.1016/j.tecto.2003.08.008.

Gunawan, R. M. P. P., G. Ikhwanushova, A. Harijoko et al. (2021). Re-interpretation of distribution of Lautan Pasir caldera-forming eruption products, Bromo-Tengger Caldera Complex, East Java, IOP Conference Series: Earth Environmental Science, 851, 1, 012038, doi:10.1088/1755-1315/851/1/012038.

Hall, R. (2002). Cenozoic geological and plate tectonic evolution of SE Asia and the SW Pacific: Computer-based reconstructions, model and animations, J. Asian Earth Sci., 20, 4, 353-431, doi:10.1016/S1367-9120(01)00069-4.

Hamilton, W. B. (1979). Tectonics of the Indonesian region (Professional Paper No. 1078; Professional Paper). U.S. Geological Survey, doi:10.3133/pp1078.

Hariyono, E. and S. Liliasari (2018). The Characteristics of Volcanic Eruption in Indonesia. In G. Aiello (Ed.), Volcanoes – Geological and Geophysical Setting, Theoretical Aspects and Numerical Modeling, Applications to Industry and Their Impact on the Human Health. InTech, doi:10.5772/intechopen.71449.

Hendrayana, H., I. A. Riyanto and A. Nuha (2024). Karakteristik Hidrogeologi dan Hidrogeokimia DAS Tempuran Lereng Barat Kompleks Gunungapi Bromo-Tengger. Majalah Geografi Indonesia.

Heriawan, M. N., R. A Hafizsyah, J. S. Hanunah, A. N. H. Hede and D. Malik (2020). Surface and Subsurface Fracture Zones Modeling Using Automatic Lineament Analysis and Geostatistical Method, with Case Study of Wayang Windu Geothermal Field, West Java, Indonesia. IOP Conference Series: Earth and Environmental Science, 417, 1, 012007, doi:10.1088/1755-1315/417/1/012007.

Hilyah, A., N. Dwi Riyantiyo and W. Utama (2017). Soil Vulnerability Analysis Using Microtremor Data In Tengger Caldera, Bromo Tengger Semeru National Park. Proceeding of The 7th Annual Basic Science International Conference, 147-150.

Ibrahim, K., S. Bijaksana, M. Abdurrachman, D. P. Sahara, et al. (2025). Contrasting magmatic structures and tectonic controls from integrated gravity and magnetic data in the Bromo-Tengger-Semeru complex and the Lamongan Volcanic Field, East Java, Indonesia, J. Volcanol. Geoth. Res., 468, 108455, doi:10.1016/j.jvolgeores.2025.108455.

Isaaks, E. H. and R. M. Srivastava (1989). Applied geostatistics, Oxford University Press. https://global.oup.com/academic/product/an-introduction-to-applied-geostatistics-9780195050134?q=Geostatistics&lang=en&cc=us.

Kane, M. F. (1962). A comprehensive system of terrain corrections using a digital computer, Geophys., 27, 4, 455-462, doi:10.1190/1.1439044.

Lestari, W., A. Hilyah, F. Syaifuddin, J. P. G. N. Rochman et al. (2017). Identifikasi Sedimen Piroklastik Pada Kawah Tengger Gunung Bromo Menggunakan Metode Resistivitas 2D, Jurnal Geosaintek, 3, 2, 115. doi:10.12962/j25023659.v3i2.2967.

Lunt, P. (2019). The origin of the East Java Sea basins deduced from sequence stratigraphy, Mar. Petrol. Geol., 105, 17-31, doi:10.1016/j.marpetgeo.2019.03.038.

Marliyani, G. I., H. Helmi, J. R. Arrowsmith and A. Clarke (2020). Volcano morphology as an indicator of stress orientation in the Java Volcanic Arc, Indonesia, J. Volcanol. Geoth. Res., 400, 106912, doi:10.1016/j.jvolgeores.2020.106912.

Maryanto, S., A. K. Nugraha, S. D. Wuryani, A. Prayogo et al. (2017). Temporal Changes of Complete Bouguer Anomalies at Bromo Volcano, East Java, Indonesia, Int. J. Appl. Engin. Res., 12, 21, 10867-10873.

Matheron, G. (1963). Principles of geostatistics, Economic Geol., 58, 8, 1246-1266, doi:10.2113/gsecongeo.58.8.1246.

Miller, C. A., J. Barretto, J., V. Stagpoole, F. Caratori-Tontini, et al. (2022). The integrated history of repeated caldera formation and infill at the Okataina Volcanic Centre: Insights from 3D gravity and magnetic models. J. Volcanol. Geoth. Res., 427, 107555, doi:10.1016/j.jvolgeores.2022.107555.

Morelli, C., C. Gantar, R. McConnell, B. Szabo and U. Uotila (1972). The International Gravity Standardization Net 1971 (I.G.S.N.71). 0192.

Moritz, H. (1980). Geodetic reference system 1980, Bull. Géodésique, 54, 3, 395-405, doi:10.1007/BF02521480.

Mulyadi, F. (Degree-grantor), Eddy; Camus, Guy (Advisor (for a thesis or dissertation), Université de Clermont-Ferrand 2, Clermont-Ferrand. (1992). Le complexe de Bromo-Tengger (Est Java, Indonésie). Etude structurale et volcanologique.

Nagy, D. (1966). The gravitational attraction of a right rectangular prism, Geophys., 31, 2, 362-371, doi:10.1190/1.1439779.

Njandjock, P., C. Kenfack, A. Diab Diab, K. Njeudjang et al. (2013). A geostatistical re-interpretation of gravity surveys in the Yagoua, Cameroon region, Geofísica Internacional, 52, 4, 365-373, doi:10.1016/S0016-7169(13)71483-1.

Oliver, M. A. and R. Webster (2014). A tutorial guide to geostatistics: Computing and modelling variograms and kriging, Catena, 113, 56-69, doi:10.1016/j.catena.2013.09.006.

Pratiwi, R. N. J., A. A. Martha, H. Hartono, R. Wijayanti et al. (2026). Identification of Subsurface Geological Structures of the Arjuno-Welirang Geothermal Potential Area Using the Gravity Method. Malaysian J. Fundamen. Appl. Sci., 22, 1, 90-101, doi:10.11113/mjfas.v22n1.4573.

Rachmawati, T. A., D. Rahmawati and A. Rachmansyah (2018). Disaster risk analysis of Mount Bromo eruption after the 2015 eruption in Sukapura District. MATEC Web of Conferences, 229, 01015, doi:10.1051/matecconf/201822901015.

Rochman, J. P. G. N., W. Nurdiansyah Buwonokeling, M. Haris Miftahul Fajar, A. Hilyah et al. (2024). Comparison of Airborne Magnetic and Ground Magnetic for Identification of Sub-surface Condition Study Case Sand Caldera

of Bromo-Tengger Volcanic Complex: Preliminary Study, IOP Conference Series: Earth and Environmental Science, 1418, 1, 012061, doi:10.1088/1755-1315/1418/1/012061.

Rouhani, S. (Ed.). (1996). Geostatistics for environmental and geotechnical applications, ASTM, https://www.astm.org/stp1283-eb.html.

Sabrian, P. G., A. Saepuloh, K. Koike, M. R. Septyandy et al. (2024). Geostatistical multitemporal InSAR method and elastic deformation model for detailed characterizations of topographic change and magma reservoirs: Application to the Tangkuban Parahu Volcano, Indonesia, J. Volcanol. Geoth. Res., 445, 107964, doi:10.1016/j.jvolgeores.2023.107964.

Santosa, S. and T. Suwarti. (1992). Peta Geologi Lembar Malang [Map].

Satyana, A. H. (2005). Oligo-Miocene carbonates of Java, Indonesia: Tectonic-volcanic setting and petroleum implications, Proc. Indon Petrol. Assoc., 30th Ann. Conv. Thirtieth Annual Convention, doi:10.29118/IPA.1592.05.G.031.

Setiadi, I. (2012). Lithological density distribution of Mount Tampomas, West Java. Pusat Survei Geologi, Badan Geologi Kementerian ESDM.

Smyth, H. R., R. Hall, J. Hamilton and P. D. Kinny (2005). East Java: Cenozoic Basins, Volcanoes and Ancient Basement, https://api.semanticscholar.org/CorpusID:55101940.

Smyth, H. R., R. Hall and G. J. Nichols (2008). Cenozoic volcanic arc history of East Java, Indonesia: The stratigraphic record of eruptions on an active continental margin. In Special Paper 436: Formation and Applications of the Sedimentary Record in Arc Collision Zones, 436, 199-222, Geological Society of America, doi:10.1130/2008.2436(10).

Solikhin, A., J.-C. Thouret, A. Gupta, A. J. L. Harris and S. C. Liew (2012). Geology, tectonics, and the 2002-2003 eruption of the Semeru volcano, Indonesia: Interpreted from high-spatial resolution satellite imagery, Geomorph., 138, 1, 364-379, doi:10.1016/j.geomorph.2011.10.001.

Spector, A. and F. S. Grant (1970). Statistical models for interpreting aeromagnetic data, Geophys., 35, 2, 293-302, doi:10.1190/1.1440092.

Sukir, M., A. Meidi, S. Vanisa and T. Hetty (2017). Polarization of Volcanic Tremor Recorded at Bromo Volcano, East Java, Indonesia, Int. J. Appl. Environ. Sci, 12, 11, 1993-2005, https://www.ripublication.com/ijaes17/ijaesv12n11_11.pdf.

Toulier, A. (2020). Multidisciplinary study for the characterization of volcanic aquifers hydrogeological functioning: Case of Bromo-Tengger volcano (East Java, Indonesia) [Hydrosciences Montpellier]. https://theses.hal.science/tel-02488883.

Untung, M. and H. Hasegawa (1982). Gravity and Geological Studies in the Tengger Caldera, East Java, Bull. Geol. Res. Develop.Centre, 6, 1-10.

Valentin, O., N. N. Philippe, B. Dieudonné, D. A. Diab and M.-D. Eliézer (2012). A Geostatistical Approach to Map Gravity Data Over Logone-Birni Sementary Basin (Chad-Cameroon), European J. Scient. Res., 93, 2, 183-189, https://www.academia.edu/5990258/A_Geostatistical_Approach_to_Map_Gravity_Data_Over_Logone_Birni_Sementary_Basin_Chad_Cameroon_A_Geostatistical_Approach_to_Map_Gravity_Data_Over_Logone_Birni_Sementary_Basin_Chad_Cameroon_184.

Van Gerven, M. and H. Pichler (1995). Some aspects of the volcanology and geochemistry of the Tengger Caldera, Java, Indonesia: Eruption of a K-rich tholeiitic series, J. Southeast Asian Earth Sci., 11, 2, 125-133, doi:10.1016/0743-9547(95)00003-B.

van Padang, M. N. and I. V. Association (1951). Catalogue of the Active Volcanoes of Indonesia, International Volcanological Association, https://books.google.co.id/books?id=clOyGwAACAAJ.

Venzke, E. (2016). Report on Tengger Caldera (Indonesia), Bull. Global Volcan. Net., 41, 12, doi:10.5479/si.GVP.BGVN201612-263310.

Wackernagel, H. (2003). Multivariate Geostatistics, Springer Berlin Heidelberg, doi:10.1007/978-3-662-05294-5.

Wardoyo, A., J. Noor, G. Elbers, S. Schmitz et al. (2020). Characterizing Volcanic Ash Elements from the 2015 Eruptions of Bromo and Raung Volcanoes,Indonesia, Polish J. Environmental Studies, 29, 2, 1899-1907, doi:10.15244/pjoes/99101.

Wuryani, S. D., S. Maryanto and A. Nadhir (2014). Identifikasi Kantung Magma Gunung Bromo Berdasarkan Analisa Sebaran Hiposenter Gempa VTA. Brawijaya Physics Student Journal, https://media.neliti.com/media/publications/160372-ID-identifikasi-kantung-magma-gunung-bromo.pdf.

Xie, J., J. Huang, J. Lu, G. J. Burton et al. (2022). Development of two-dimensional ground models by combining geotechnical and geophysical data, Engin. Geol., 300, 106579, doi:10.1016/j.enggeo.2022.106579.

Zaennudin, A. (2011). Perbandingan antara erupsi Gunung Bromo Tahun 2010-2011 dan erupsi Kompleks Gunung Tengger, Jurnal Lingkungan dan Bencana Geologi, 2, 1, 21-37.

Zaennudin, A., R. D. Hadisantono, R. D. Erfan and A. R. Mulyana (1994). Peta Geologi Gunungapi Bromo-Tengger, Jawa Timur [Map]. Pusat Penelitian dan Pengembangan Geologi.

Zaennudin, A., K. Kristianto, E. Lusy (2012). Model Erupsi Gunung Bromo di Jawa Timur pada Tahun 2010-2011. Jurnal Lingkungan dan Bencana Geologi, 3, 1, 41-55, doi:10.34126/JLBG.V3I1.35.

Zhang, X. F., J. C. H. Van Eijkeren and A. W. Heemink (1995). On the weighted least-squares method for fitting a semivariogram model, Compu. Geosci., 21, 4, 605-608, doi:10.1016/0098-3004(94)00099-G.

Zimmerman, D., C. Pavlik, A. Ruggles and M. P. Armstrong (1999)xAn Experimental Comparison of Ordinary and Universal Kriging and Inverse Distance Weighting, Math. Geol., 31, 4, 375-390, doi:10.1023/A:1007586507433.

***CORRESPONDING AUTHOR: Sismanto SISMANTO**,
Universitas Gadjah Mada, Department of Physics, Yogyakarta, Indonesia
e-mail: sismanto@ugm.ac.id
© 2026 the Author(s).
Open Access. This article is licensed under a Creative Commons Attribution 4.0 International License